3D Simulation of Vajont Disaster. Part 1: Numerical Formulation and Validation

Alessandro Franci[a], Massimiliano Cremonesi[b], Umberto Perego[b], Giovanni Crosta[c], Eugenio Oñate[a]

[a]*International Center for Numerical Methods in Engineering (CIMNE), Universitat Politècnica de Catalunya (UPC), Carrer Gran Capitán, UPC Campus Nord, Barcelona*
[b]*Politecnico di Milano, Department of Civil and Environmental Engineering, Piazza Leonardo da Vinci 32, Milan, Italy*
[c]*Università degli Studi di Milano Bicocca, Department of Earth and Environmental Science, Piazza della Scienza, 4, Milan, Italy*

Abstract

This work presents a numerical method for the simulation of landslides generated impulse waves and its application to the historical Vajont case study. The computational tool is based on the Particle Finite Element Method (PFEM), a Lagrangian strategy that combines the finite element solution of the governing equations with an efficient remeshing strategy to deal with large deformation problems. After presenting the numerical formulation, different landslide impulse wave problems with Froude number ranging from 0.5 to 2.8, are analyzed to validate the proposed methodology. The computational method is shown to be able to reproduce accurately the landslide runout, the momentum transfer between the sliding material and the impounded water, and the consequent wave propagation observed in experimental physical models. Then, the PFEM model is applied to the numerical simulation of the Vajont disaster, which is analyzed with a fully-resolved three-dimensional model. The numerical results are discussed and compared to the post-event observations and the numerical results of other computational methods. The results in terms of landslide velocity and runout, geometry of the deposit, maximum water runup, dam overtopping wave, and water discharge in the downstream valley are in good agreement with observations and reconstructions. The calibration and validation performed for this study form the basis for the PFEM analyses presented in a companion paper finalized to simulate different scenarios of the Vajont rockslide considered in the experimental tests done a year before the disaster.

Keywords:
Rockslide, Rock Avalanche, Vajont, Particle Finite Element Method, PFEM, Impulse Wave

1. Introduction

Landslides are responsible for significant human and economic losses worldwide (Froude and Petley, 2018). Between 1995 and 2014, landslides caused over 160,000 deaths and 11,000 injured worldwide (Haque et al., 2019) and, only considering 27 European countries, an approximated economic loss of 4.7 billion Euros (Haque et al., 2016). According to World Bank data (Dilley et al., 2005), about 300 million people live in landslides-prone areas. Global warming effects, the intensification of extreme rainfalls and new settlements in risk areas, driven by the rise of the world population, are contributing to increasing the number of deadly landslides worldwide (Haque et al., 2019). This critical scenario puts in the foreground the urgency of improving the current predicting techniques for this major natural hazard.

Due to the complexity of landslide dynamics and the difficulty in defining the material properties and behavior, predicting landslide effects on natural and human environments is a hard endeavor. This task is even more complicated when landslides are accompanied by other natural hazards in a cascading mode, as in the case of landslides falling into water reservoirs and generating impulse waves. Depending on the slide initial position, geometry, material, velocity, evolution, and water reservoir characteristics, tsunami-type waves may form and affect the shoreline of the reservoirs.

The fjord area of western Norway is one of the world regions most susceptible to this type of natural hazard (Harbitz et al., 2014). In this area, rock avalanches and associated tsunamis caused more than 170 casualties during the last 100 years (Blikra et al., 2005). The most tragic event occurred in Tajford in 1934, when a massive rockslide of around 3 million cubic meters dropped into the fjord resulting in a devastating flood wave that washed over $60m$ on the opposite shorelines and the nearby Tafjorden communities (Braathen et al., 2014).

More recently, landslide induced tsunami waves were recorded in Greenland (Gauthier et al., 2018; Paris et al., 2019; Bloom et al., 2019), where the seriousness of this type of phenomena can become more and more relevant considering present-day climate changes, especially at high latitudes.

The highest recorded wave runup produced by a landslide occurred on July 9^{th} 1958 at the head of Lituya Bay on the southern coast of Alaska (Miller, 1960; Fritz et al., 2009). On that occasion, an 8.3 magnitude earthquake along the Fairweather fault triggered a major rockslide which, after impacting the water of the lake, generated a giant tsunami and a water runup of $524m$ (Fritz et al., 2001).

The landslide impulse wave event of Vajont (northern Italy) was the one with the highest number of associated casualties (around 2000). On the night of October 9^{th} 1963, about 275 million cubic meters of rock detached from the northern side

of the Mount Toc, slumped on the water basin and produced a massive water runup of around $200m$ on the opposite flank of the valley (Semenza, 1965, 2002, 2010; Semenza and Ghirotti, 2010; Ghirotti, 2012; Paronuzzi et al., 2013). A significant part of the huge impounded water volume overtopped the dam and, after traveling about $1.5km$ through the Vajont gorge, reached the Piave valley destroying almost entirely the village of Longarone (Viparelli and Merla, 1968; Ward and Day, 2011). As highlighted by serveral authors (Hendron and Patton, 1985; Semenza, 2002; Alonso and Pinyol, 2010), the catastrophic Vajont landslide consisted of the reactivation of an ancient landslide that was triggered by the filling–drawdown cycles of the Vajont reservoir and heavy rains occurring in the same period. According to Paronuzzi et al. (2013), the variation of reservoir level caused a decrease in the slope factor of safety (FOS) up to 12% of the initial value (already close to the critical conditions, FOS ≈ 1.14), while the maximum decrease in FOS associated with rainfall was estimated to about 4%.

The critical issues related to landslide impulse-wave events make more and more desirable the implementation of new technologies for improving the predictive capabilities of current forecasting methods. The recent advancements in hardware and numerical technologies put computational methods in the foreground for this objective. However, the numerical simulation of these multi-hazard scenarios is still challenging. Indeed, even assuming the failure surface and the initial volume of the landslide as known, the computational method must be able to track the deforming shape of the landslide during the runout, to reproduce carefully its complex constitutive behavior, to limit mass variations, and to be applicable to large-scale three-dimensional (3D) geometries based on real topographic data. Furthermore, in case of landslides impacting onto water reservoirs, the numerical tool must be able to deal with severe topological changes undergone by the water (splashes and breaking waves), and to have good mass and energy conservation properties to reproduce accurately the momentum transfer at the impact and the consequent wave propagation.

Lagrangian approaches have several advantages versus traditional Eulerian methods to solve large deformation problems as landslide impulse-wave events. Thus, while Lagrangian strategies track naturally the deforming shape of the computational domain, Eulerian methods require additional tools, such as Level Set (Osher and Fedkiw, 2002) or Volume of Fluid (Hirt and Nichols, 1981) methods. On the other hand, mesh-based Lagrangian methods may lead to mesh distortion when applied to large deformation problems (Zienkiewicz et al., 2005). This issue is naturally overcome by Lagrangian meshless methods, such as the Smooth Particle Hydrodynamics (SPH) (Gingold and Monaghan, 1977), the Lattice Boltzmann Method (LBM) (Chen and Doolen, 1998) and the Discrete Element Method (DEM) (Cundall and Strack, 1979). In the SPH, the computational domain is discretized into Lagrangian particles over which the material properties are smoothed by kernel functions. The LBM divides the space into regular lattices and solves the kinetic Boltzmann equations over the particle distribution functions defined for each lattice. Finally, in a DEM approach, the particles move according to the second Newton's law, taking into account the contact forces between particles and the effect of the fluid on particle motion (buoyancy and drag forces). Examples of applications of SPH, LBM and DEM techniques to landslides impulse wave problems can be found in McDougall and Hungr (2004); Minatti and Pasculli (2011); Pastor et al. (2015, 2009), Pak and Sarfaraz (2014); Qiu et al. (2019), and Zhao et al. (2016); Shan and Zhao (2014), respectively.

The Material Point Method (MPM) still uses Lagrangian particles to follow the deforming domain, but, unlike the particle-methods presented above, adopts a background Eulerian mesh for solving the governing equations with the Finite Element Method (FEM) (Sulsky et al., 1994). This hybrid Eulerian-Lagrangian nature confers the possibility of using complex constitutive laws for the landslide material and, at the same time, the capability of tracking the deforming shape of the triggered material. These features explain the considerable attention gained by the MPM in the last two decades in the field of landslides modeling (Pinyol et al., 2017; Andersen and Andersen, 2010; Soga et al., 2016; Yerro et al., 2016, 2019).

Unlike all the previously mentioned particle-based methods, the Particle Finite Element Method (PFEM) (Idelsohn et al., 2004; Oñate et al., 2004; Larese et al., 2008) uses a Lagrangian mesh to solve the governing equations as in standard FEM. The issue of mesh distortion is overcome through an efficient remeshing strategy based on an enhanced Delaunay Triangulation algorithm (Edelsbrunner and Tan, 1993; Edelsbrunner and Mucke, 1999). The combination of the FEM solution of the governing equations with the treatment of mesh nodes as material particles makes of the PFEM a suitable method for large deformation problems, including the numerical simulation of landslides (Zhang et al., 2015, 2017) and their interaction with water reservoirs (Cremonesi et al., 2011; Salazar et al., 2012, 2016; Cremonesi et al., 2017; Zhang et al., 2019; Mulligan et al., 2020).

This work aims to show the effectiveness of the PFEM for simulating complex 3D landslide impulse wave events. After presenting and validating the PFEM technique against some well-known benchmarks, the computational method is applied to the simulation of the Vajont disaster.

In the last two decades, several numerical strategies have been applied to model the Vajont disaster. Zaniboni and Tinti (2014) subdivided the rockslide into six sub-slides and their motion was computed with a one-dimensional (1D) Lagrangian model. A two-dimensional (2D) Discontinuous Deformation Analysis was used by Sitar et al. (2005) to analyze the rockslide failure. Thermal effects on the Vajont sliding velocity were studied by Pinyol et al. (2017) using a 2D MPM model. The Vajont rockslide and the consequent impulse wave were analyzed in 2D by Zhao et al. (2016) using a DEM-CFD (Computational Fluid Dynamics) method and by Manenti et al. (2016, 2018) using SPH. The hydraulic analysis of the Vajont disaster was the main focus of the shallow-water model used by Bosa and Petti (2011, 2013), while the rockslide was modeled as a prescribed boundary condition. A similar choice was adopted by Vacondio et al. (2013), who modeled the landslide as a rigid body with assigned motion, while water was simulated with a 3D SPH model. The so-called Tsunami Balls method (Ward and

Day, 2008) was used by Ward and Day (2011) to simulate the landslide and the consequent water motion, including the flow over the dam and the flooding of the Piave valley. Nevertheless, at the best of the authors' knowledge, the only fully 3D simulation of the Vajont disaster was presented by Crosta et al. (2016), where both water and landslide were modeled with a 3D Arbitrary Lagrangian-Eulerian (ALE) method (Crosta et al., 2006, 2009). In this work, the Vajont case study is analyzed with the PFEM using a 3D fully-resolved model and, at the best of our knowledge, with the highest mesh resolution ever published. In a companion paper (Franci et al., 2020), hypothetical scenarios of the Vajont disaster are analyzed and related to the pre-event experimental predictions of Ghetti (1962).

The paper is structured as follows. In Section 2, the PFEM-based numerical model used in this work is presented. First, the governing equations and the constitutive models are described, and then, the PFEM algorithm is explained. Section 3 is dedicated to the validation of the method against two benchmark experimental tests for landslide impulse wave problems. Finally, Section 4 presents the Vajont case study and discusses the results of the 3D numerical simulations. The conclusions of the work are given in Section 5.

2. Numerical formulation

2.1. Balance equations

In this work, both the landslide material and the water are analyzed in a fluid dynamics framework. The governing equations are solved in an updated Lagrangian description as in the standard Particle Finite Element Method (PFEM). These equations are the linear momentum balance and mass conservation and they read

$$\rho \frac{\partial v_i}{\partial t} - \frac{\partial \sigma_{ij}}{\partial x_j} - b_i = 0 \quad \text{in } \Omega_t \times (0,T) \tag{1}$$

$$\frac{1}{\kappa}\frac{\partial p}{\partial t} + \frac{\partial v_i}{\partial x_i} = 0 \qquad \text{in } \Omega_t \times (0,T) \tag{2}$$

where ρ is the bulk density of the material (either the landslide or the water), v_i is the i^{th} component of the velocity field, t is the time, σ_{ij} is ij^{th} component of the Cauchy stress tensor, b_i is the i^{th} component of the body force per unit of volume, κ is the material bulk modulus, p is the pressure, Ω_t is the updated computational domain, and T is the total duration of the analysis.

We remark that the mass conservation equation (Eq.2) is not solved with the divergence-free form of the standard Navier-Stokes problem ($\frac{\partial v_i}{\partial x_i} = 0$), but admitting a small (practically, negligible) compressibility controlled by the material bulk modulus (Idelsohn et al., 2008; Ryzhakov et al., 2012; Franci et al., 2015).

The Cauchy stress tensor is computed as the sum of its deviatoric and volumetric parts as

$$\sigma_{ij} = \tau_{ij} - p\delta_{ij} \tag{3}$$

where τ_{ij} is ij^{th} component of the deviatoric stress tensor and δ_{ij} is the Kronecker delta.

For both landslide material and water, the deviatoric part of the Cauchy stress can be written as

$$\tau_{ij} = \bar{\mu}\dot{\gamma}_{ij} \tag{4}$$

where $\bar{\mu}$ is the apparent viscosity (defined for each constitutive model in Section 2.2) and $\dot{\gamma}_{ij}$ is the deviatoric strain rate, which, assuming as negligile the volumetric strain rate, is computed from the velocities as

$$\dot{\gamma}_{ij} = \frac{\partial v_i}{\partial x_j} + \frac{\partial v_j}{\partial x_i} \tag{5}$$

To close the problem, appropriate initial and boundary conditions must be defined.

2.2. Constitutive model

Water is modeled as a standard Newtonian fluid with a constant and uniform apparent viscosity $\bar{\mu}$ (Eq.(4)) that coincides with the fluid dynamic viscosity μ. Hence:

$$\bar{\mu} = \mu \tag{6}$$

For the landslide material, a frictional viscoplastic model inspired on the Bingham model has been used. The Bingham model has been largely used for modeling geophysical flows, such as mudflows, debris flows and lahars (Pastor et al., 2015). The shear stress of a Bingham material is defined for a steady case as

$$\begin{aligned} &\tau_{ij} = \tau_0 \frac{\dot{\gamma}_{ij}}{|\dot{\gamma}|} + \mu\dot{\gamma}_{ij} && \text{for } |\tau| \geq \tau_0 \\ &\dot{\gamma}_{ij} = 0 && \text{for } |\tau| < \tau_0 \end{aligned} \tag{7}$$

where τ_0 is the shear yield stress and $|\dot{\gamma}|$ is the equivalent strain rate which is computed as

$$|\dot{\gamma}| = \sqrt{\frac{1}{2}\dot{\gamma}_{ij}\dot{\gamma}_{ij}} \tag{8}$$

.

To overcome the well-known numerical drawbacks of the standard Bingham model, the previous power law is regularized with an exponential function (Papanastasiou, 1987). For a general 3D case, this regularized model reads

$$\tau_{ij} = \left[\mu + \frac{\tau_0}{|\dot{\gamma}|}\left(1 - e^{-m|\dot{\gamma}|}\right)\right]\dot{\gamma}_{ij} \tag{9}$$

where m is the regularization parameter.

For problems in which the effect of friction is not negligible, a frictional viscoplastic model is used. In this case, the above viscoplastic model is modified defining a non-constant yield limit as follows

$$\tau_0 = c + p\, tan(\phi) \tag{10}$$

where c is the cohesion and ϕ is the material friction angle.

This modification is commonly used for the flow of materials that follow a Mohr-Coulomb type criterion (Quecedo et al.,

2004; Larese et al., 2012; Salazar et al., 2016). It is worth remarking that this mono-phase model lacks the concept of effective stresses. Consequently, p represents the pressure of the landslide material rather than the effective pressure of the soil skeleton.

Combining Eq.(9) and Eq.(10), the following frictional viscoplastic model is obtained

$$\tau_{ij} = \left[\mu + \frac{c + p\,tan(\phi)}{|\dot{\gamma}|}\left(1 - e^{-m|\dot{\gamma}|}\right)\right]\dot{\gamma}_{ij} \qquad (11)$$

2.3. PFEM solution algorithm

In this work, the dynamics of both the water and landslide material are solved with the PFEM (Idelsohn et al., 2004; Oñate et al., 2004). The method is based on a fully Lagrangian strategy designed to solve large deformation problems. The solution of each time step is obtained with a FEM solver, while mesh distortion issues are managed with an efficient remeshing strategy combining the Delaunay Triangulation with a topological method for real-time definition of the computational boundaries. In the following, the FEM solution strategy and the remeshing procedure used in this PFEM formulation are briefly described.

2.3.1. FEM solver

The governing equations Eqs.(1-2) are discretized with a standard Galerkin finite element approach using tetrahedral elements with linear interpolation for both velocities and pressure unknowns. For the transient solution we use the implicit stabilized scheme proposed in Oñate et al. (2014). The method is based on a two-step velocity-pressure scheme and uses a Finite Increment Calculus (FIC) stabilization (Oñate, 1998; Oñate et al., 2014; Pouplana and Oñate, 2017) to avoid the spurious oscillations induced by the unfulfillment of the *inf-sup* condition (Brezzi and Fortin, 1991). Details can be found in in Oñate et al. (2014), Franci et al. (2015), and Franci and Zhang (2018).

For a generic time step $[^n t; ^{n+1} t]$ of duration Δt, the momentum balance and mass conservation equations are solved in time iteratively for the increments of nodal velocities and pressures according to the following algorithm.

At each non-linear iteration k:

1. Compute nodal velocity increments $\Delta\bar{v}$: $K^k \Delta\bar{v} = R(\bar{v}^k, \bar{p}^k)$
2. Update nodal velocities: $^{n+1}\bar{v}^{k+1} = {}^{n+1}\bar{v}^k + \Delta\bar{v}$
3. Update nodal coordinates: $^{n+1}\bar{x}^{k+1} = {}^{n+1}\bar{x}^k + \bar{u}(\Delta\bar{v})$ being $\bar{u}$ the nodal displacements.
4. Compute nodal pressures $\bar{p}^{k+1}$: $H^k \bar{p}^{k+1} = F_p(\bar{v}^{k+1}, \bar{p}^k)$
5. Update Cauchy stress: $\sigma^{k+1} = \tau(\bar{v}^{k+1}) - p^{k+1} I$
6. Check convergence: $\dfrac{\|\Delta\bar{v}^{k+1}\|}{\|^n\bar{v}\|} \leq e_v$, $\dfrac{\|\bar{p}^{k+1} - \bar{p}^k\|}{\|^n\bar{p}\|} \leq e_p$ with e_v and e_p prescribed error norms for velocities and pressures.

If condition 6 is not fulfilled, return to 1 with $k \leftarrow k+1$.

All variables marked with an upper bar refer to nodal values. The vectors and matrices introduced in the previous algorithm are detailed in Appendix A.

2.3.2. Lagrangian mesh management

In Lagrangian approaches, such as the PFEM, the mesh nodes move according to the FEM solution of the governing equations, as explained in Sections 2.1-2.2. However, as shown in Figs. 1a- 1b, this may lead to an excessive distortion of the mesh when large deformation problems are solved.

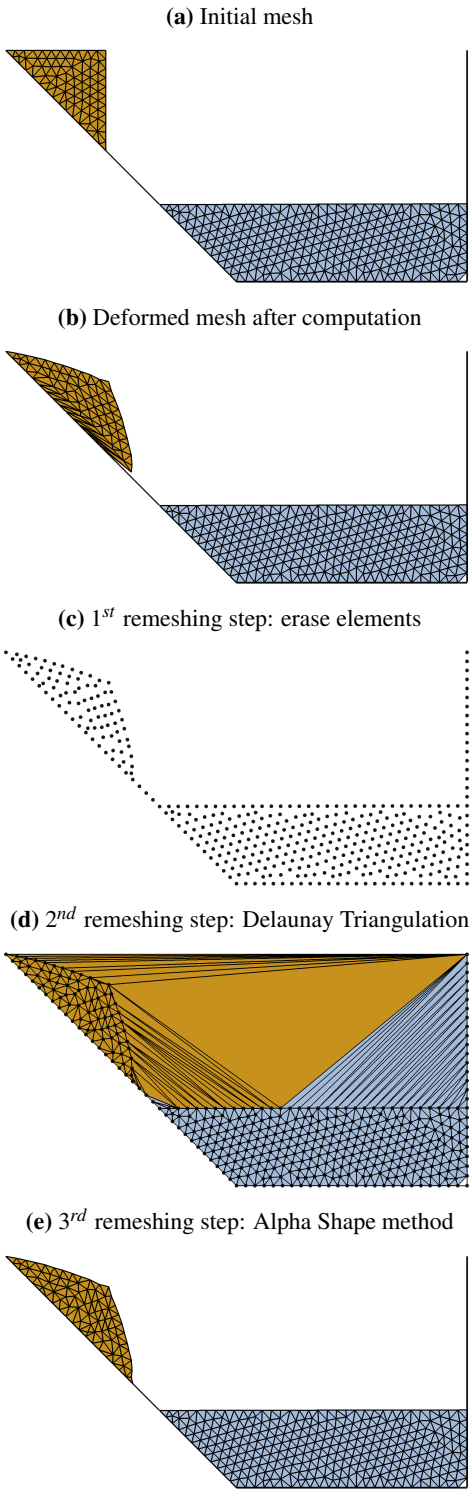

(a) Initial mesh

(b) Deformed mesh after computation

(c) 1^{st} remeshing step: erase elements

(d) 2^{nd} remeshing step: Delaunay Triangulation

(e) 3^{rd} remeshing step: Alpha Shape method

Figure 1: PFEM solution algorithm for a large deformation problem. (a)-(b) Mesh distortion due to computation. (c)-(e) Remeshing steps.

Thus, whenever the mesh exceeds a pre-fixed distortion level, a new discretization is built over the nodes of the previous (distorted) mesh, redefining the elemental connectivity (Idelsohn et al., 2004). This is done in the PFEM with a three-step procedure (Figs. 1c- 1e). First, all the elements of the distorted mesh are removed (Fig. 1c), and the problem information is stored at the nodes. Then, a new mesh is built over this cloud of points by performing a Delaunay triangulation (Edelsbrunner and Tan, 1993) (Fig. 1d). Finally, in order to recover the actual contours of the computational domain, the so-called Alpha Shape method (Edelsbrunner and Mucke, 1999) is applied (Fig. 1e). During this step, all the elements that are considered excessively distorted according to a prefixed criterion are removed from the discretization. The resulting mesh is now ready to be used for the FEM solution of the next computational time step. More details of the PFEM procedure can be found in Idelsohn et al. (2003), Oñate et al. (2004), Franci and Cremonesi (2017), and Cremonesi et al. (2020).

3. Validation tests

In this section, the proposed PFEM technique is validated in the context of submarine landslides and tsunami wave generation against the experimental tests of Rzadkiewicz et al. (1997) and Fritz (2002).

In the first analysis, a saturated sand submarine landslide was modeled with a 3D regularized Bingham model. In the second one, the impact of a granular mass against a water reservoir and the subsequent wave were reproduced.

3.1. Subaqueous sandflow

The submarine landslide reproduced in one of the experimental tests of Rzadkiewicz et al. (1997) is here simulated numerically with the proposed PFEM model. The fully submerged sliding mass is composed of saturated sand and it is placed over a slope with inclination 45°. Following Rzadkiewicz et al. (1997), a Bingham model was used for the landslide using the following material parameters: $\rho = 1985 kg/m^3$, $\tau_0 = 200 Pa$, and $\mu = 0.001 Pa \cdot s$. A regularization parameter $m = 1000 s^{-1}$ was adopted. Water was modeled as a Newtonian fluid using $\rho = 1000 kg/m^3$ and $\mu = 0.001 Pa \cdot s$. For this test, the Froude number $Fr = v_s/(gh)^{0.5}$, being v_s the sliding velocity and h the reservoir height, is estimated equal to 0.5. No-slip conditions between the sliding mass and the inclined surface are assumed. Fig. 2 shows a graphical representation of the initial geometry of the test.

The problem was solved with both 2D plane strain and 3D models. The initial mesh had 16,574 triangles in the 2D case and 749,165 tetrahedral elements in the 3D model. In both cases, a mean mesh size of 2.75 *cm* was used.

A lateral view of the 3D numerical results obtained at $t = 0.4s$ and $t = 0.8s$ is given in Fig. 3. The landslide body reached peak velocities of around $2m/s$ before depositing over the lower horizontal plane. As shown in the figure, the sliding of landslide material induces the motion of the water contained in the tank perturbating its free-surface contour.

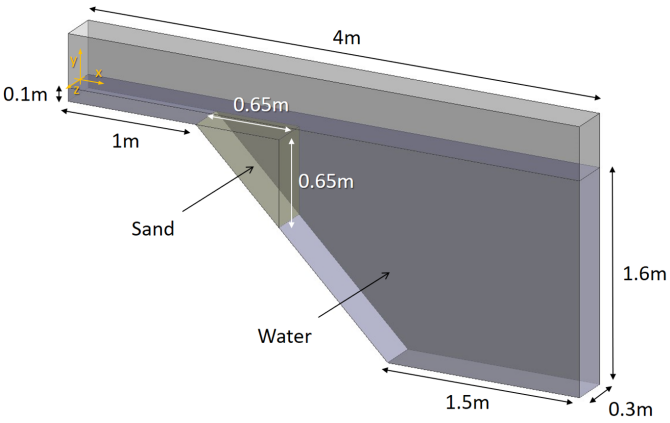

Figure 2: Subaqueous sandflow. Initial geometry.

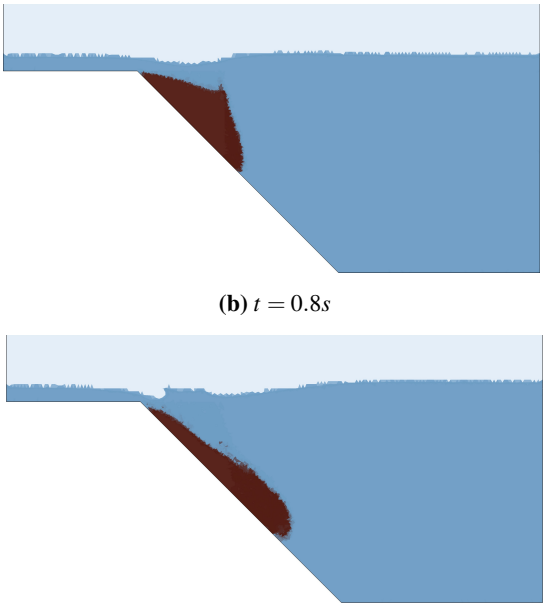

Figure 3: Subaqueous sandflow. Numerical results at $t = 0.4s$ and $t = 0.8s$.

The profile of the upper water surface obtained experimentally at $t = 0.4s$ and $t = 0.8s$ (Rzadkiewicz et al., 1997) is plotted in Fig. 4 together with the results given by a 2D SPH model (Rzadkiewicz et al., 1997) and those obtained here with the PFEM.

The graphs show an overall good agreement between the 3D PFEM results and the experimental observations. Instead, the 2D analyses with SPH and PFEM, although showing good mutual agreement, have clear discrepancies versus the experimental values. These results confirm the potential of the PFEM for this type of problems and its agreement with literature results. Moreover, they show the relevance of 3D effects in landslide events and, thus, the importance of using 3D models for their numerical simulation.

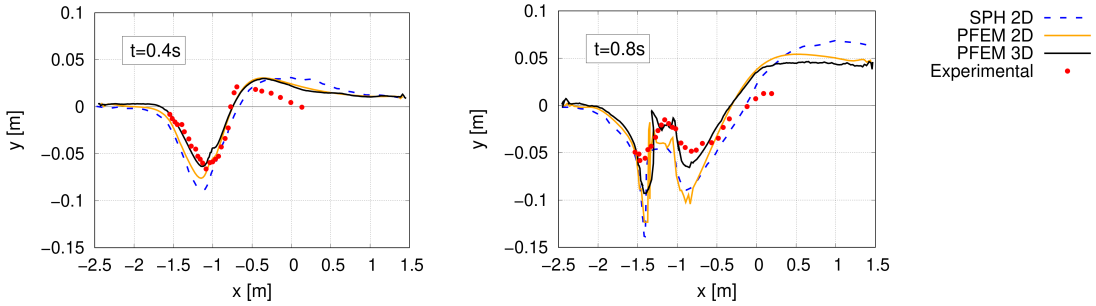

Figure 4: Position of water free-surface at two time instants. Experimental values and SPH results from Rzadkiewicz et al. (1997).

3.2. Granular slide impact and wave generation

This test aims to analyze the suitability of the proposed PFEM model for the simulation of impulse waves generated by the impact of landslides. For this purpose, the series of experiments presented in Fritz (2002) was considered. In these experimental tests, different masses of granular material were made to slide on an inclined plane and to impact the water at rest placed in the underlying tank. Different shapes and initial velocities of landslides were studied in the laboratory tests. In this section, only two cases of the experimental series are analyzed. In the first test, the sliding material has an initial length $d = 0.3m$ and zero velocity. This analysis aimed to verify only the accuracy of the used model for frictional material. For this reason, water is not modeled and only the landslide motion is analyzed. In the second test, also water is simulated and, a larger mass ($d = 0.6m$) with an initial velocity of $3.17m/s$ was considered for the sliding material. For both cases, 2D plane strain conditions were assumed in the numerical simulations. In terms of slide Froude number, Fritz (2002) estimated $Fr = 1.7$ for the first test and $Fr = 2.8$ for the second one. Due to the relevance of frictional effects, the granular material was modeled with the frictional viscoplastic law of Eq.(11). The model was fed with the material parameters provided in Fritz (2002), using a friction angle of 43°, a density of $1620kg/m^3$, and a null viscosity for the sliding material. The basal plane was modeled with a reduced friction angle of 24° following Fritz (2002) and considering no-slip conditions. A possible alternative to accounting for the different behavior of the basal surface could be using Navier slip conditions (see *e.g.* Cremonesi et al. (2017)).

Fig. 5 shows the initial geometry of the tests together with the auxiliary coordinates (x;y) and (x^*;y^*) and the location of the four probes used to monitor the sliding material motion and the water wave amplitude.

Concerning the mesh, a very fine mesh (mean element size of $5mm$) was used for both tests. In the first one, the whole model was discretized with 3,210 3-noded triangles, while in the second test, 6,420 and 113,000 linear triangular elements were used for discretizing the granular material and the water, respectively.

3.2.1. Subareal slide motion

Fig. 6 shows for the first case ($Fr = 1.7$) the time evolution of the height of the granular mass measured at probe P1 (Fig. 5).

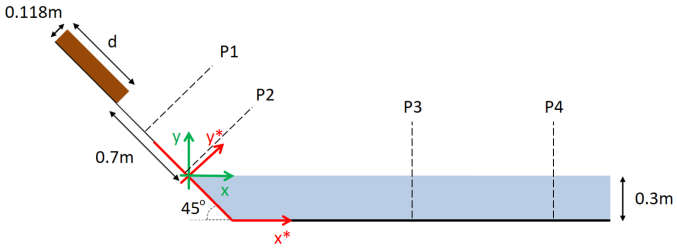

Figure 5: Granular slide impact and wave generation modeling setup. The subareal slide motion is monitored at probes P1 and P2 ($x^* = -0.4m$ and $-0.07m$, respectively). The water wave amplitude is measured at probes P3 and P4 ($x = 1.43m$ and $2.43m$, respectively).

In the graph, both numerical and experimental results are plotted, and, for both, $T = 0$ is the time instant at which the height of the sliding mass at the measuring point P1 reaches the 25% of the initial height. The graph shows a very good agreement be-

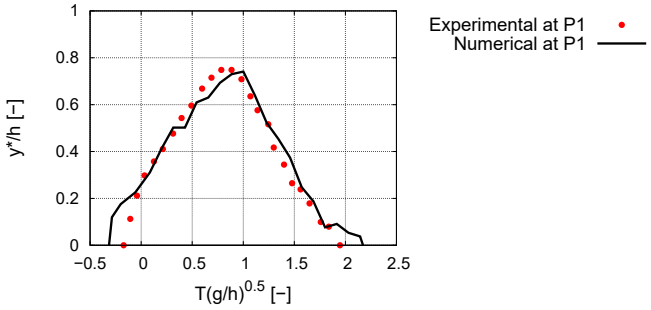

Figure 6: Time evolution of sliding material height measured at probe P1 of Fig. 5. Results for the test with $Fr = 1.7$. Comparison to experimental observations of Fritz (2002).

tween the numerical results and the experimental observations. The duration and maximum height of the landslide are very well captured by the numerical method proving the accuracy of the frictional model.

In the second test ($Fr = 2.8$), the height of the sliding granular mass was measured also at P2, placed very close to the water reservoir. Fig. 7 shows the time evolution of the numerical and experimental profiles at the measuring points P1 and P2.

In this case, although the numerical model captures well the

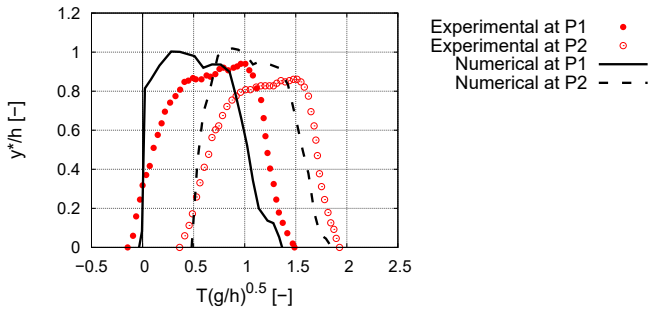

Figure 7: Time evolution of sliding material height measured at probes P1 and P2 of Fig. 5. Results for the test with $Fr = 2.8$. Comparison to experimental observations of Fritz (2002).

landslide duration and timing, the numerical results seem to be less accurate than in the first test. This disagreement is probably due to the inaccurate modeling of the initial sliding conditions. In particular, the initial tangent velocity $v_i = 3.17m/s$ was imposed to all the nodes of the granular mass. This may be not representative of the initial landslide kinematic conditions given by the pneumatic acceleration mechanism used in the experiments.

3.2.2. Impact and subaqueous slide motion

Fig. 8 shows a qualitative comparison of numerical and experimental results at the impact zone. Both in the experiment and in the simulation, the initial time $t = 0$ represents the impact moment, which, in the numerical simulation, happens after $0.175s$ from the landslide release. Despite some discrepancies, the pictures show an overall good qualitative agreement between the numerical and the experimental results. In particular, the PFEM model can reproduce the initial flow separation (Fig. 8a), the following backward collapsing impact crater (Figs. 8b-8c), and the formation and propagation of the major wave (Fig. 8d).

(a) $t(g/h)^{0.5} = 0.72$

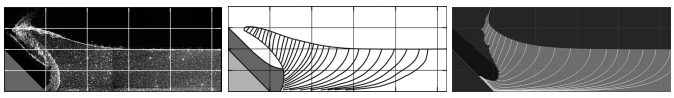

(b) $t(g/h)^{0.5} = 2.24$

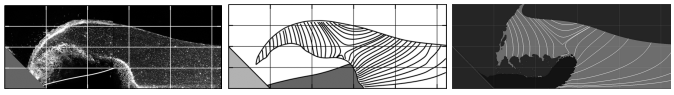

(c) $t(g/h)^{0.5} = 3.77$

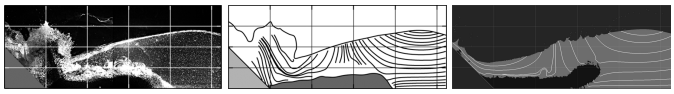

(d) $t(g/h)^{0.5} = 4.53$

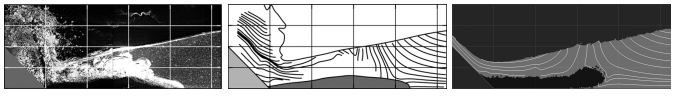

Figure 8: Granular slide impact and wave generation. Left column: experimental observations (Fritz, 2002). Central column:water streamlines (Fritz, 2002). Right column: PFEM results.

In Fritz (2002), the following normalized relations for the subaqueous landslide duration and runout obtained from multiple regressions (Ratkowsky, 1990) were provided.

$$\begin{aligned} x^*/h &= 3.7\left(v_s/\sqrt{gh}\right)^{0.3}\left(V_s/\sqrt{dh^2}\right)^{0.3} \\ t\sqrt{g/h} &= 5.2\left(v_s/\sqrt{gh}\right)^{-0.2}\left(V_s/\sqrt{dhs}\right)^{0.3} \end{aligned} \tag{12}$$

where v_s, V_s and s are the slide impact velocity, volume and thickness, respectively.

Fig. 9 compares the obtained normalized subaqueous landslide duration and runout (measured data) with the values obtained with Eqs.(12). The observations of the experimental test obtained in Fritz (2002) are plotted in the same graph. The pictures show a very good agreement between the obtained results and the experimental regression formula.

(a) Landslide runout

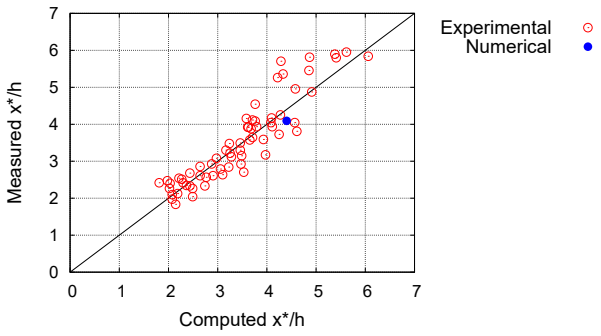

(b) Landslide duration

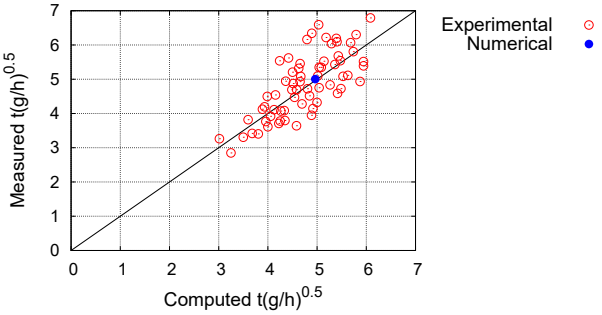

Figure 9: Granular subaqueous landslide runout and duration. PFEM results, experimental observation of Fritz (2002) and computed values from Eqs.(12).

3.2.3. Wave propagation

Fig. 10 shows the normalized time evolution of the normalized wave amplitude at $x = 1.43m$ (P3) and $x = 2.43m$ (P4).

Both numerical and experimental results are reported. As for the subaqueous slide analysis, the impact time instant is considered as the initial time $t = 0$ for both numerical and experimental analyses. The graphs show a general agreement of the

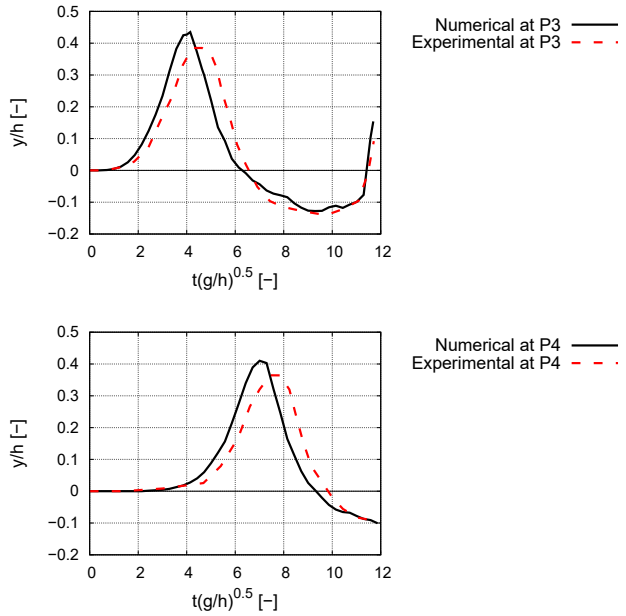

Figure 10: Wave amplitude measured at probes P3 and P4 (Figure 5). Experimental results from Fritz (2002).

numerical results with the experimental observations, although the numerical analysis slightly overestimates the velocity and the maximum amplitude of the wave. Looking at these results it should be considered that material permeability and 3D effects were neglected in the numerical model, and both these assumptions have the effect of overestimating the impact force of the landslide.

4. Case study: Vajont disaster

The Vajont rockslide occurred on October 13^{th} 1963 during the drawdown of the hydroelectric reservoir when the water altitude was at about $700m$ above sea level (*a.s.l.*) (Semenza, 1965). The sliding mass had an estimated volume of about 275 million cubic meters (Selli and Trevisan, 1964; Ciabatti, 1964; Datei, 1969; Viparelli and Merla, 1968) and a characteristc M-shape given by two main volumes with similar shape (west and east lobes). The Massalezza creek flowing down from the Mount Toc divided the two blocks, as shown in Fig. 11.

According to several authors (Muller, 1964; Selli and Trevisan, 1964; Ciabatti, 1964; Voight and Faust, 1982; Hendron and Patton, 1985; Nonveiller, 1987), the rockslide moved some 360-450m to north and 140m upwards on the opposite valley with an estimated maximum velocity of 15-30m/s. The rockslide front thickness was comparable to (or even larger than) the depth of the water reservoir, causing the complete displacement of the water body from the reservoir. Based on these observations, the Froude number of the Vajont rockslide can be estimated as ranging between 0.26 and 0.75 (Crosta et al., 2016).

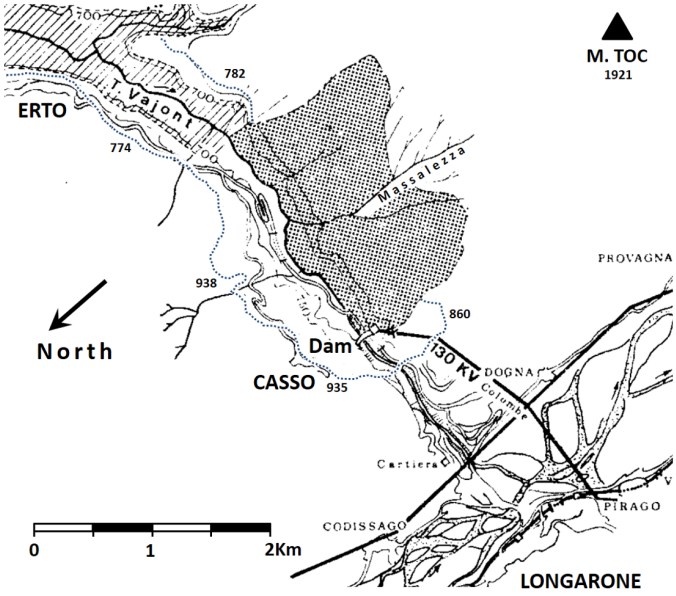

Figure 11: Vajont valley map before the landslide (edited from Viparelli and Merla (1968)).

About 170 million cubic meters of water were pushed upwards over the northern flank of the valley eroding the soil up to an elevation of about $950m$ *a.s.l.* (Semenza, 1965).

Part of the impounded water (about $25 \cdot 10^6 m^3$ according to Selli and Trevisan (1964); Viparelli and Merla (1968)) overtopped the dam crest ($725m$ *a.s.l*) with an estimated flow rate of about $10^5 m^3/s$ (Viparelli and Merla, 1968). Another part of the wave came back towards the mobilized landslide material, and a third part moved eastward in the upstream direction as a tsunami wave propagating in the residual Vajont lake towards the Erto village.

A summary of the observed and estimated magnitudes of the Vajont disaster is given in Table 1.

4.1. Computational domain and mesh

The Vajont rockslide and consequent impulsive water wave were reproduced with a 3D PFEM model. The geometry of the landslide body was the same as the one used in Crosta et al. (2016). The sliding volume was reconstructed starting from the pre- and post-failure topographic information obtained by topographic data, geological maps and cross sections by Rossi and Semenza (1965) and (Rossi and Semenza, 1986), Lidar surveys (provided by the Regione Friuli Venezia Giulia), borehole data (Broili, 1967), and field checks.

Fig. 12 shows the computational domain at its initial configuration. From a top view, the area of study is a $4km \times 3km$ rectangle. As shown in the picture, the origin of (x,y) reference system is placed at the easternmost point of the dam, at a distance in x-direction of $795m$ from the northernmost point of the computational domain, and $710m$ in the y-direction from the westernmost one. Fig. 12 also shows the eight sections that will be used in the following study to analyze specific aspects of the

Table 1: Vajont case study. Summary of observations data.

Magnitude	Value and reference
Landslide volume $[m^3]$	$270\text{-}300 \cdot 10^6$ (Selli and Trevisan, 1964; Ciabatti, 1964; Viparelli and Merla, 1968; Datei, 1969)
Landslide duration $[s]$	20-25 (Caloi, 1966), 30-45 (Muller, 1964), 45 (Selli and Trevisan, 1964; Ciabatti, 1964)
Landslide velocity $[m/s]$	15-20 (Selli and Trevisan, 1964; Ciabatti, 1964; Nonveiller, 1987), 20-30 (Muller, 1964; Voight and Faust, 1982; Hendron and Patton, 1985)
Water runup $[m]$	200-250 (Viparelli and Merla, 1968)
Water flow $[m^3/s]$	about $100 \cdot 10^3$ (Viparelli and Merla, 1968)
Flooded volume $[m^3]$	about $25 \cdot 10^6$ (Selli and Trevisan, 1964; Viparelli and Merla, 1968)

multi-hazard event dynamics. Section A is placed at $x = 0m$, while sections B, C, D, E, F, G and H are located at $y = 0m$, $500m$, $870m$, $1700m$, $2240m$, 2450, and $2840m$, respectively. Sections A and B are used to analyze the wave overtopping the dam, sections C, D and E to monitor the sliding velocity of the rockslide, and sections F, G and H to measure the amplitude of the tsunami wave propagating in the residual lake.

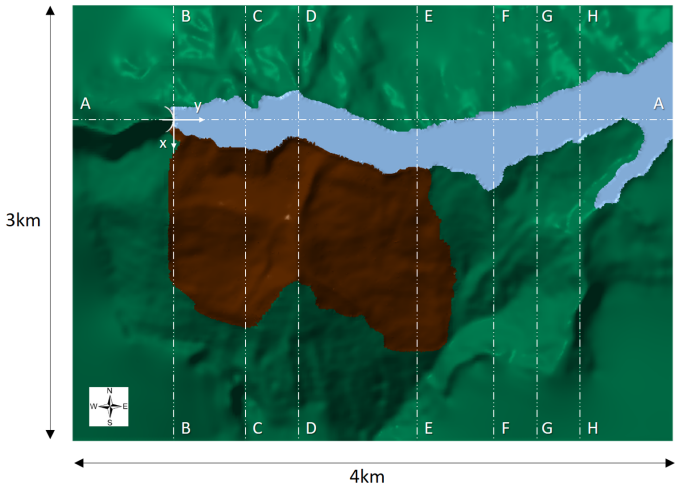

Figure 12: Computational domain considered for the Vajont analysis and position of cross-sections.

The crest of the dam has an altitude of about $725m$ *a.s.l.* and the initial water level is placed at $700m$ *a.s.l.*, which was the actual reservoir level at the time of the disaster.

Space was discretized with a finite element mesh with a mean element size of $10m$. Remarkably, this mesh size is almost half of that used in the only other 3D analysis of the Vajont disaster available in the literature (Crosta et al., 2016). At the beginning of the computations, the landslide volume is discretized with around 2,800,000 tetrahedral elements, while around 1,120,000 tetrahedra are used for the water reservoir. The mountain and the dam surfaces are discretized with 242,738 and 1,411 linear triangular elements, respectively. Fig. 13 shows a detailed view of the mesh used.

All the numerical analyses were run for an overall time duration of $100s$.

4.2. Material parameters

The rockslide was solved with the regularized frictional visco-plastic model of Eq.(11). Two different values of friction angle were used for the landslide material and the basal

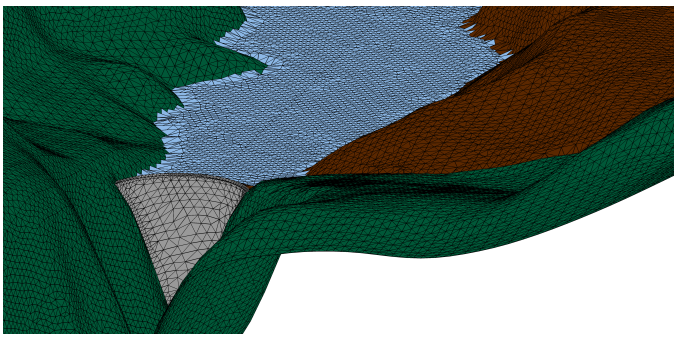

Figure 13: Detail of the PFEM mesh. View from behind the dam.

surface. For the bulk landslide material, friction and cohesion were taken equal to $\phi_{lan} = 34^\circ$ and $c_{lan} = 1000kPa$, respectively. For the basal surface, a lower value of friction was used, namely $\phi_{bas} = 11^\circ$. It is important to note that the values of friction angles and cohesion are the same as the residual ones used in Pinyol et al. (2017) and the reduced friction angle of the landslide basal plan (11°) fit into the ranges 4°-23°, 5°-16° and 2°-36° proposed for the failure surface in Tika and Hutchinson (1999), Hendron and Patton (1985) and Ferri et al. (2011), respectively. A density $\rho_{lan} = 2400kg/m^3$ has been considered for the landslide material. Water was modeled as a standard Newtonian fluid with dynamic viscosity $\mu_f = 0.001Pa \cdot s$ and density $\rho_f = 1000kg/m^3$. Finally, the mountain and the dam were modeled as fixed rigid bodies.

As in the other fully 3D analysis of the Vajont disaster (Crosta et al., 2016), no-slip conditions were considered for the mountain and the dam surfaces.

4.3. Overall dynamics

Fig. 14 shows the 3D PFEM results at eight time instants taken at regular time intervals of $10s$. The pictures show that the PFEM can reproduce the main phenomena occurred in the Vajont disaster, such as the detachment, spread, and stoppage of the landslide (Figs. 14a-14d), the consequent impounding water wave and runup on the opposite valley flank (Figs. 14a-14e), the water overtopping of the Vajont dam (Figs. 14c-14h), and the generation and propagation of the tsunami wave through the residual lake (Figs. 14d-14h). Within the duration of the analysis ($100s$), the numerical simulation does not show the formation of the small Massalezza lake over the deposited rockslide, observed after the event (Bosa and Petti, 2011).

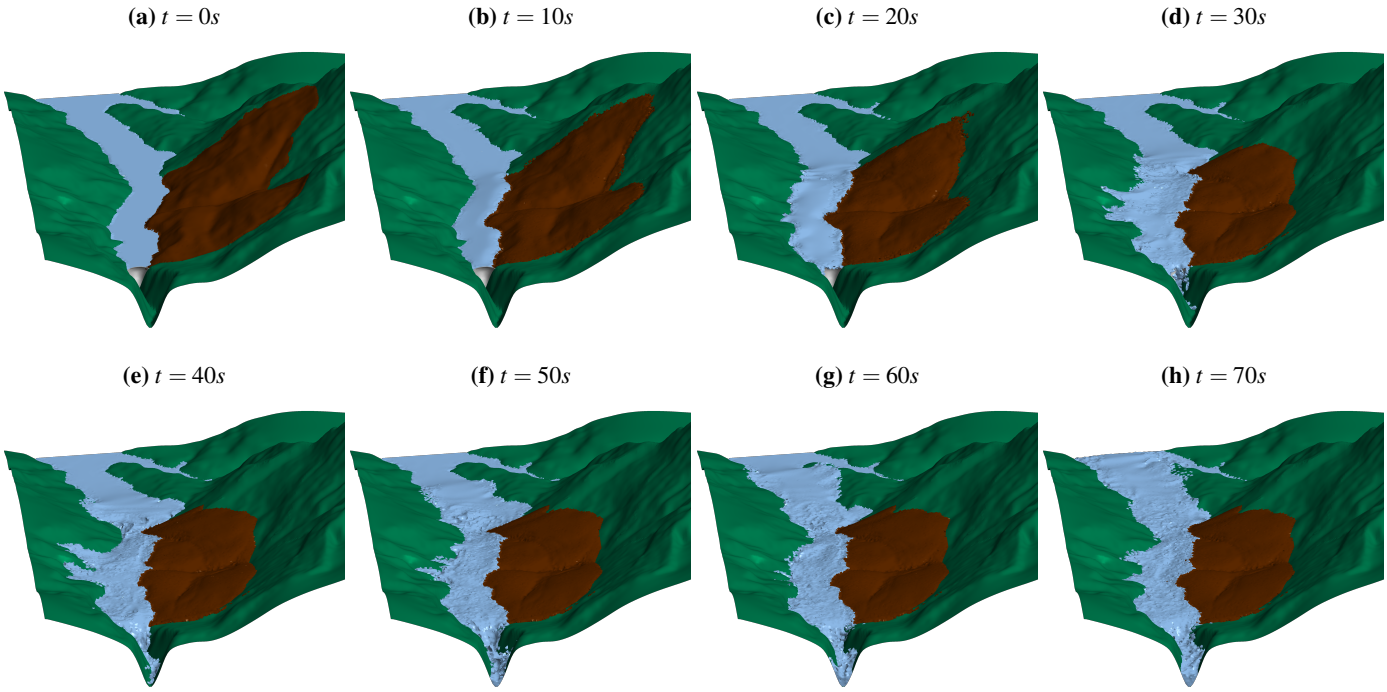

Figure 14: PFEM Results of the simulation of the Vajont disaster at eight time instants. View from the dam side (*i.e.* from east).

4.4. Landslide dynamics

Fig. 15 shows a zenithal view of the PFEM numerical results for the velocity field. For the sake of clarity, the post-process velocity contours are shown with a fixed limit of $40m/s$, beyond which the dark red color is used.

The pictures show clearly the motion of the landslide against the water initially at rest and the progressive stoppage of the mobilized mass.

From a general view of landslide velocities, the higher values are obtained at the top of the sliding material, as also reported by Crosta et al. (2016). The maximum velocities at the landslide front are around $15m/s$, while at the top the velocities are of the order 25-$30m/s$, with even higher local peak values.

The maximum sliding velocities are obtained between $15s$ and $25s$ and are experienced at its eastern part (Figs. 15c-15e), where peak values of almost $40m/s$ were reached. The faster motion of the eastern part of the landslide was already highlighted in Crosta et al. (2016), where similar values of velocities were obtained. For the rest of the landslide, the obtained velocities are in agreement with what is reported in the literature (see Table 1).

Regarding the sliding duration, Fig. 15f shows that after $30s$ most of the rockslide already stopped and some motion was still occurring only at its eastern side. This is confirmed by Fig. 16 plotting the results of sections C, D and E at four different time steps. The sections cut the landslide body at three different zones: in particular, section C at the western lobe, section D in correspondence with Massalezza creek, and section E at the eastern lobe (see Fig. 12).

The pictures show that at $t = 35s$ the landslide body has an almost zero velocity at every section allowing to estimate a land-

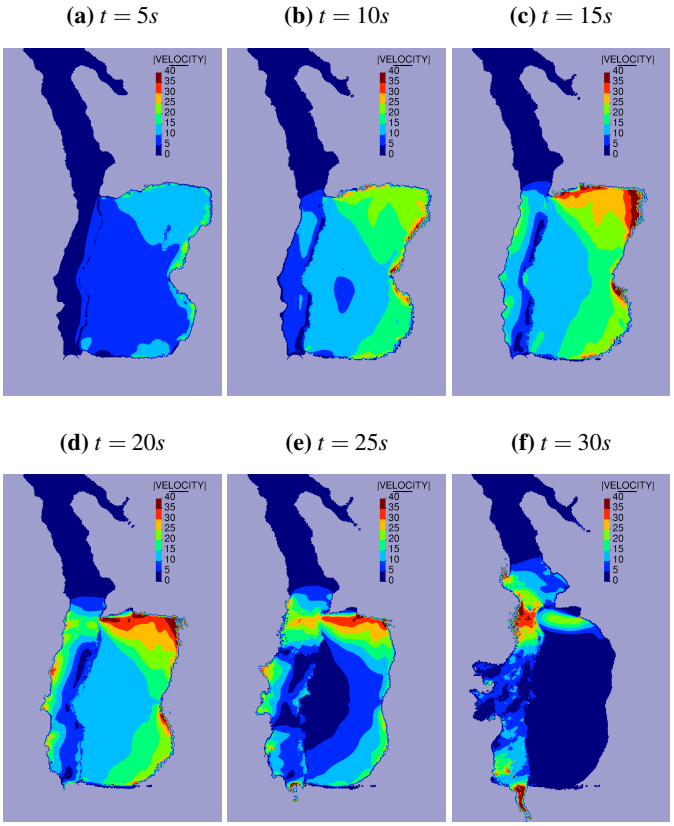

Figure 15: Plan view of the Vajont computational domain with plot of velocity vector modulus results (velocity upper limit of $40m/s$).

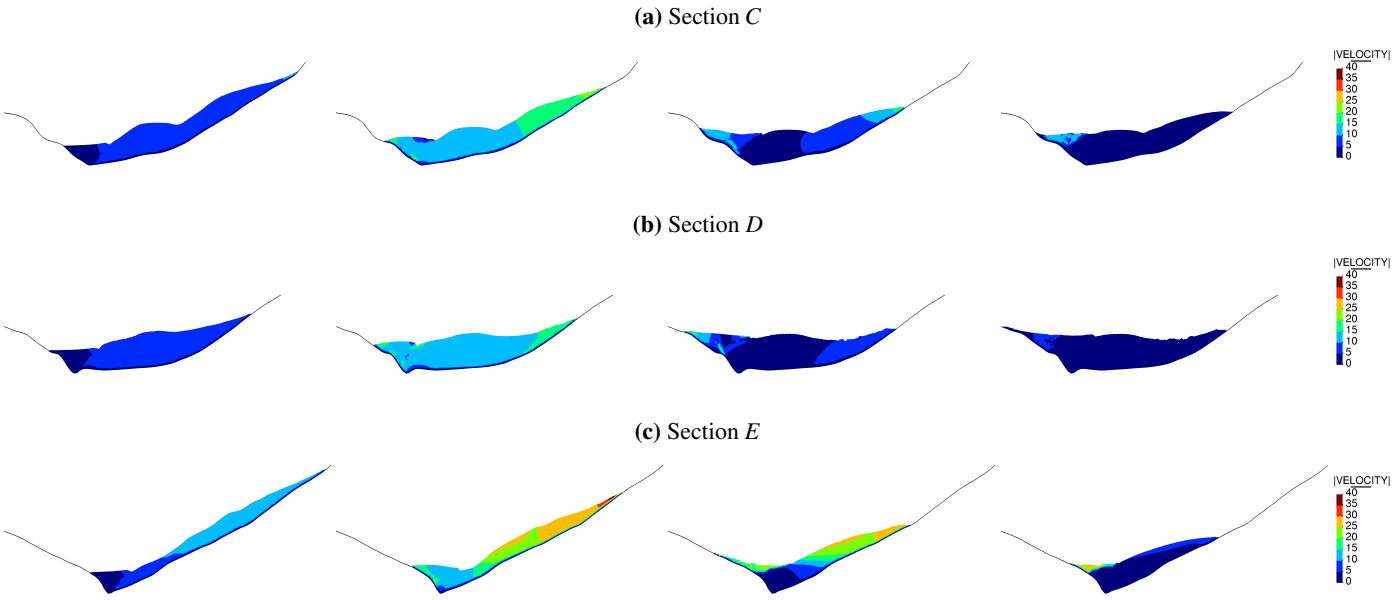

Figure 16: Results at sections C, D and E of the Vajont computational domain given in Fig. 12. Velocity results at four time instants: $t = 5s$, $t = 15s$, $t = 25s$, and $t = 35s$, from the left to the right (velocity upper limit of $40m/s$).

slide duration of around 30-35s, a time interval that agrees with the considerations of Muller (1964).

The results of Fig. 16 also show that the Vajont landslide has a clear three-dimensional behavior. Indeed, the motion and the velocities of the western lobe (Fig. 16a) are much different from the ones at the eastern lobe (Fig. 16c).

4.5. Landslide deposit

Fig. 17 plots the final deposit obtained with the PFEM together with the one measured after the rockslide event (Semenza, 1965) and the results of the other 3D Vajont model in the literature (Crosta et al., 2016). The results show an overall good agreement between the numerical results and the observed data, although there are some discrepancies, especially at the southern boundary (uphill) of the landslide. There, the numerical model gives a much flatter landslide surface and a less clear separation between lobe east and west than the one shown by the observed data. A similar behavior was also obtained with the ALE FEM model of Crosta et al. (2016), although it must be taken into account that in that work the mesh size was almost twice the one used in this PFEM analysis.

4.6. Upstream propagating wave

The propagation of a huge wave in the Vajont residual lake was responsible for important human and economic losses on the shoreline of the reservoir. The village that was most affected by this tsunami wave was Erto (Fig. 11), placed at about 1.5km upstream.

The numerical results show that the first main wave starts propagating in the lake after around 25s from the rockslide detachment (Fig. 15e). At that time, the impounded mass of water is still moving upwards on the northern flank of the Vajont valley, as shown in Fig. 18a plotting the velocity vectors at $t = 30s$

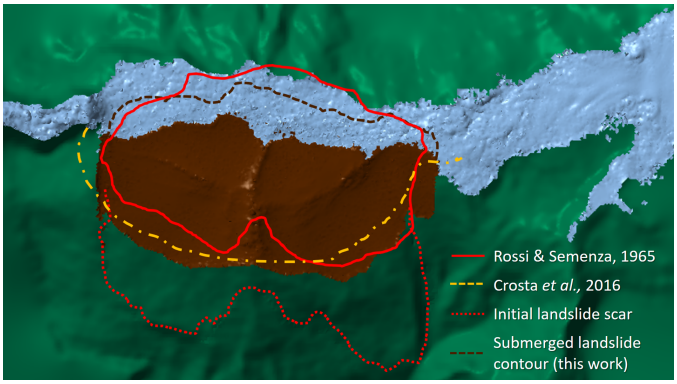

Figure 17: Final Vajont landslide deposit. Comparison with observed data of Rossi and Semenza (1965) and the numerical results of (Crosta et al., 2016).

(the maximum runup is reached at around $t = 35s$, as it will be shown in Section 4.8). These results suggest that the first main wave propagating upstream was produced directly by the first push of the rockslide onto the water reservoir and not by the impact of the impounded water volume coming down from the northern valley flank, which occurred some seconds later, between $t = 40s$ and $t = 60s$ (Figs. 18b-18d). Fig. 18 is also helpful to perceive the crucial effect on the tsunami wave given by the push of the easternmost part of the rockslide (Figs. 18a-18b), as it is confirmed by the analyses of the companion paper (Franci et al., 2020) analyzing the solely collapse of the eastern lobe of the rockslide.

The main wave takes only around 50s to cover the 1.5km separating the eastern boundary of the landslide and the limit of the computational domain, resulting in an impressive average velocity of $30m/s$. After around 75s from the landslide triggering, the main wave on the Vajont reservoir reaches the village

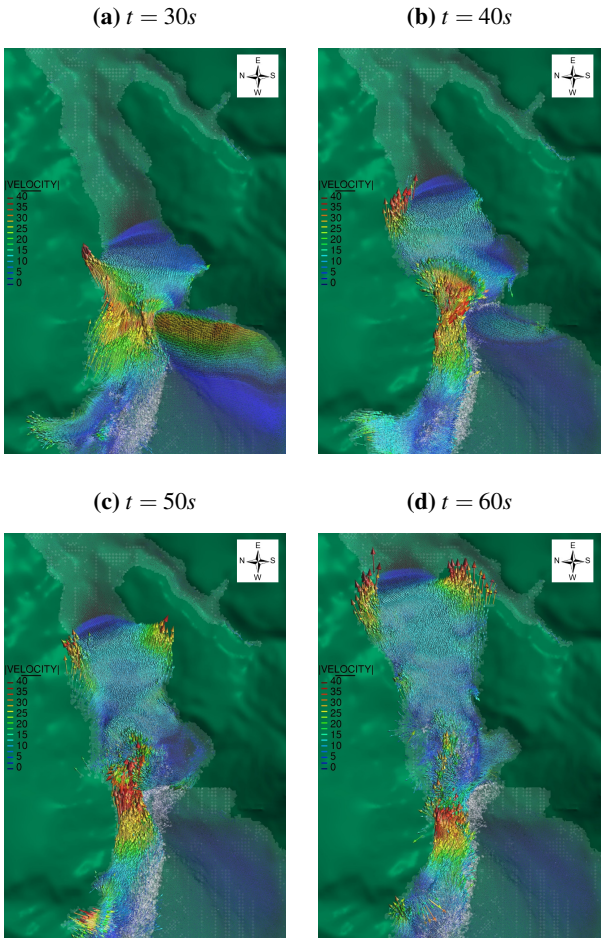

Figure 18: Wave propagating upstream in the residual Vajont lake (east direction). Zoom on the eastern side of the Vajont valley (landslide is at the bottom of the pictures and at the right hand side). Both water and landlslide material are represented with transparent color to better appreciate the velocity vectors.

of Erto, located at the north-east limit of the computational domain (Fig. 11). This time interval agrees well with that obtained in Ward and Day (2011) with a tsunami ball model and in Bosa and Petti (2011) with a shallow water method.

Fig. 19 shows the time evolution of the maximum water level measured in the eastern part of the reservoir at sections F, G and H (see Fig. 12). In all cases, the water level overcomes the initial one of more than $40m$, agreeing well with the post-event observations of Viparelli and Merla (1968).

The results of section F, the closest one to the landslide, show two clear peaks, one at about $t = 45s$ and the other at around $t = 80s$. These results support the theory of the formation of two main waves in the lake: the first one generated immediately by the force applied by the sliding material on the water reservoir, and the second one generated successively by the descending water volume which was pushed by the landslide over the northern flank of the valley.

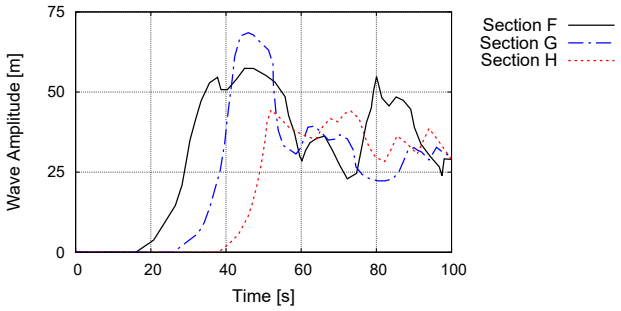

Figure 19: Time evolution of the maximum water level of Vajont reservoir at sections F, G and H of Fig. 12.

4.7. Overtopping wave

Fig. 20a shows the time evolution of water altitude above the dam. The graph shows that the overtopping of the dam crest level occurs after only around $12s$ from the rockslide release.

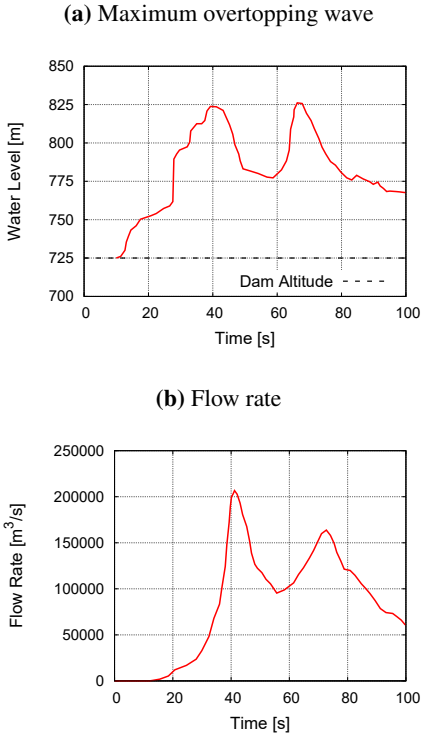

Figure 20: Time evolution of (a) maximum water level and (b) flow rate above the Vajont dam, both measured at section B of Fig. 12.

After that, two main waves take place over the dam: the first one has its maximum at around $t = 40s$, while the second one at $t = 70s$. Both overtopping waves reach peak amplitudes of around $120m$. The time evolution of the outflow rate from the dam is shown in Fig. 20b. This has been computed as the average flow rate crossing section B of Fig. 12. The flow rate graph, like the one for the overtopping wave height, shows two peaks, being the second one almost 25% smaller than the first one. The timing of both the initial overtopping wave and the

hydrograph peaks agree with the 3D results presented in Vacondio et al. (2013). The presence of two peaks in the hydrograph of outgoing water was also observed in the shallow water solution of Bosa and Petti (2011). As reported by Viparelli and Merla (1968), during the first minutes of the event, the magnitude of the water flow at the dam crest was of the order of $100 \cdot 10^3 m^3/s$, which is in line with the PFEM results.

Fig. 21a illustrates the numerical results at $t = 40s$ when the first peak of the overtopping wave is reached. The aerial view also shows the huge water runup on the northern slope and the tsunami wave propagating towards the eastern side of the valley. To better appreciate the overtopping wave, Fig. 21b plots the results on sections A and B for the same time instants. The picture shows that the central part of the reservoir is largely occupied by the mobilized landslide body.

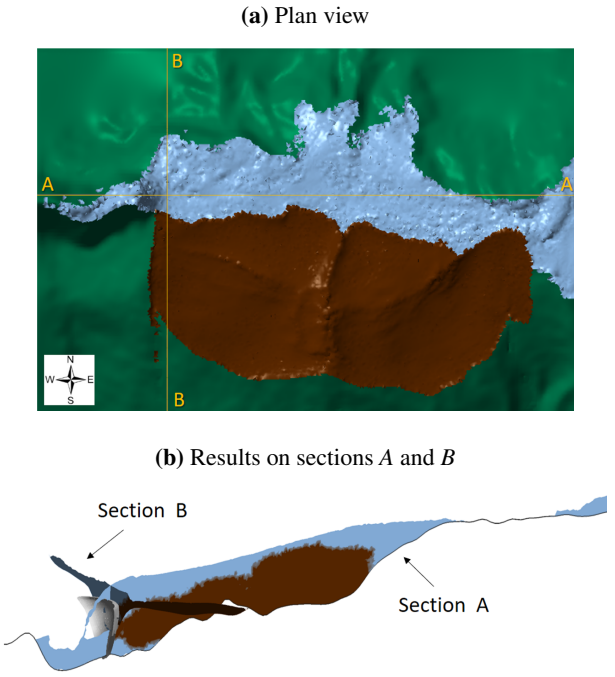

Figure 21: Results at $t = 40s$. (a) Plan view of the three-dimensional Vajont computational domain. (b) Results at sections A and B.

Fig. 21 also shows that the overtopping flow does not occur over the dam crest only but also over its lateral abutments, and, mainly, from the northern one, being the southern one occupied by the landslide body. This aspect of the outflow dynamics was also found in Bosa and Petti (2011).

4.8. Water runup

The Vajont rockslide generated an imponent water motion on the northern flank of the valley, whose profile was traced in Rossi and Semenza (1986). Fig. 22 shows the observed runup limit together with the predicted runup given by the 3D SPH method of Vacondio et al. (2013), the ALE 3D method of Crosta et al. (2016) and our PFEM model. In this work, the runup line is obtained as the envelope of the maximum northern positions reached by water at each computational step.

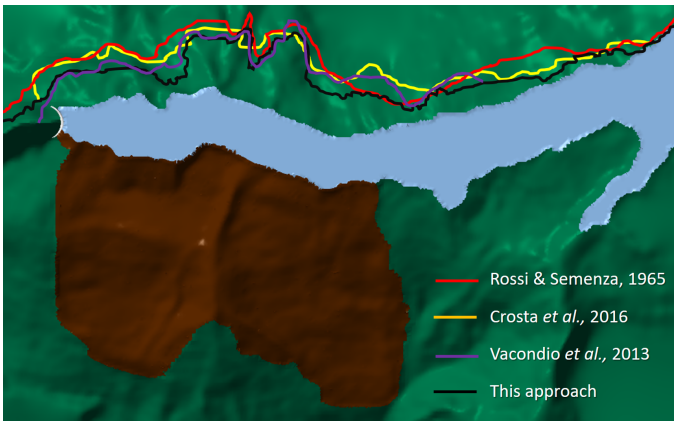

Figure 22: Water runup on the North flank of the Vajont lake. Numerical results from this PFEM approach, the SPH model of Vacondio et al. (2013) and the ALE-FEM of Crosta et al. (2016). The observed runup line Rossi and Semenza (1965) is plotted with red color.

From a general analysis, the PFEM model seems to underestimate the maximum runup in the zone close to the dam, while it captures quite well the water profile in the eastern part. Remarkably, the same behavior is shown by the results of Vacondio et al. (2013) obtained modeling the landslide as a rigid body moving at a velocity established by a retrofit analysis.

The maximum water height is reached in the central zone of the landslide, where the water reaches $910m$ $a.s.l.$, so more than $200m$ over the initial reservoir level. This value of maximum water runup is close to the post-event observations of Rossi and Semenza (1986) and Viparelli and Merla (1968), and the numerical simulations of Bosa and Petti (2011), Vacondio et al. (2013), and Crosta et al. (2016).

To better appreciate the magnitude of the runup, Fig. 23 shows the computational domain both at the initial state and at the moment of the maximum runup ($t = 35s$).

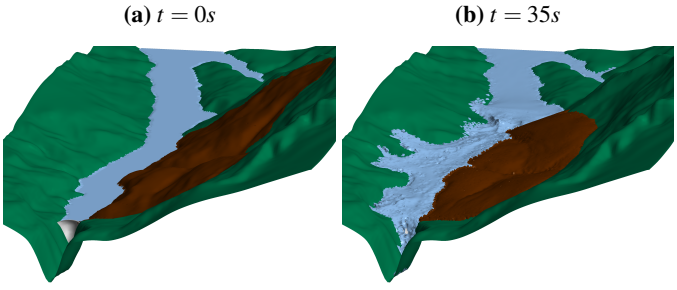

Figure 23: 3D view of the Vajont computational domain at the initial state and the time instant of the maximum runup ($t = 35s$).

5. Discussion and conclusions

This work has presented a Lagrangian computational method for the simulation of landslides impulse waves using a fluid dynamics approach. The numerical technique is based on the Particle Finite Element Method (PFEM) which combines the solution of the governing equations via the finite element method

with an efficient remeshing procedure to solve large deformation problems.

The PFEM has been first applied to benchmark experimental tests for impulse water waves generated by landslides composed of different materials. In the first test, the landslide was formed by a saturated and dense sand flow, while in the second one, the fast impact of dry granular material has been analyzed. These numerical tests were used to verify the accuracy of the regularized viscoplastic constitutive models and to assess the capability of the PFEM to deal with problems involving large topology changes of the computational domain. The numerical results were compared to experimental observations and published numerical results. In all cases, the PFEM was capable of simulating accurately the landslide motion, the interaction with the fluid and the generation and propagation of water waves, demonstrating very good energy conservation properties and the capability of dealing with large deforming computational domains, both in 2D and 3D.

One of the main objectives of the work was to show the applicability of the method to large-scale landslide events and complex scenarios. For this reason, the Vajont disaster was simulated with a fully 3D model with a fine mesh.

The PFEM showed to be capable to reproduce the main phenomena occurred in the Vajont disaster, such as the detachment, propagation, and stoppage of the rockslide, the $200m$ water runup on the opposite flank of the valley, the propagation of the tsunami wave along the residual Vajont lake and the overtopping water flow above the dam crest.

The numerical results agree with acceptable accuracy with the observations in terms of landslide velocity, duration, and final deposit, maximum water runup, and order of magnitude of the flow rate over the dam. Good agreement has been also found with other numerical methods focusing on the hydraulic part of the disaster (Vacondio et al., 2013; Bosa and Petti, 2011) and the only other fully 3D simulation of the Vajont case study (Crosta et al., 2016).

Thanks to the 3D representation of the Vajont case, this study allowed to highlight some interesting aspects of the disaster dynamics, such as the mechanism of formation of the two main water waves, the time evolution of the water outflow rate, the 3D behavior of the landslide, and the higher velocities reached in the most eastern part of the landslide. In this respect, three-dimensional models including the complete landslide geometry and realistic material properties outperform the models which introduce a simplified 1D and/or a rigid representation of the landslide, allowing to gain more insight about the real phenomena occurred during these complex multi-hazard events.

In a companion paper (Franci et al., 2020), hypothetical scenarios of the Vajont disaster obtained by varying the extent of the unstable slope (as in the pre-event experiments of Ghetti (1962)) and some of the model features and parameters, have been analyzed by the same numerical approach presented here, confirming its robustness and applicability to large-scale landslide impulse-wave scenarios.

Appendix A. Definition of matrices and vectors of PFEM solution scheme

The matrices and vectors used for the time step solution and introduced in Section 2.3.1 are given below. At each iteration, the fully discretized linear momentum equations are solved for the increments of nodal velocities as

$$K\Delta\bar{v} = R(\bar{v},\bar{p}) \tag{A.1}$$

with $K = K^m(\bar{x},c) + K^\rho(\bar{x})$, where $\bar{x}$ are the nodal coordinates, and matrices K^m and K^ρ and the residual term R are defined as follows

$$\begin{aligned} K^m_{IJ} &= \int_\Omega B_I^T c B_J d\Omega \\ K^\rho_{IJ} &= I\int_\Omega N_I \frac{2\rho}{\Delta t} N_J d\Omega \\ R_{Ii} &= \int_\Omega N_I \rho N_J d\Omega\, \bar{v}_{Ji} + \int_\Omega \frac{\partial N_I}{\partial x_j}\sigma_{ij} d\Omega - \int_\Omega N_I b_i d\Omega \end{aligned} \tag{A.2}$$

being, for 2D problems

$$c = \begin{bmatrix} \kappa\Delta t + \frac{4\bar{\mu}}{3} & \kappa\Delta t - \frac{2\bar{\mu}}{3} & 0 \\ \kappa\Delta t - \frac{2\bar{\mu}}{3} & \kappa\Delta t + \frac{4\bar{\mu}}{3} & 0 \\ 0 & 0 & \bar{\mu} \end{bmatrix},$$

$$\mathbf{B}_I^T = \begin{bmatrix} \dfrac{\partial N_I}{\partial x} & 0 & \dfrac{\partial N_I}{\partial y} \\ 0 & \dfrac{\partial N_I}{\partial y} & \dfrac{\partial N_I}{\partial x} \end{bmatrix}$$

where I is the second-order identity tensor and N are the linear shape functions.

At each non-linear iteration, the nodal pressures are obtained from the discretized continuity equation in the following form

$$H\bar{p} = F_p(\bar{v},\bar{p}) \tag{A.3}$$

with

$$H = \left(\frac{1}{\Delta t}\mathbf{M} + \frac{1}{\Delta t^2}\mathbf{M}_\tau + \mathbf{M}_{\tau b} + \mathbf{L}_\tau\right) \tag{A.4}$$

and

$$F_\tau = \frac{\mathbf{M}}{\Delta t}{}^n\bar{p} + \frac{\mathbf{M}_\tau}{\Delta t^2}\left({}^n\bar{p} + {}^n\dot{\bar{p}}\Delta t\right) - \mathbf{Q}^T\,\bar{v} + f_\tau \tag{A.5}$$

where

$$\begin{aligned} M_{IJ} &= \int_\Omega \frac{1}{\kappa} N_I N_J d\Omega \\ M_{\tau_{IJ}} &= \int_\Omega \tau\frac{\rho}{\kappa} N_I N_J d\Omega \\ M_{\tau b_{IJ}} &= \int_{\Gamma_t} \frac{2\tau}{h_n} N_I N_J d\Gamma \\ L_{\tau_{IJ}} &= \int_\Omega \tau(\nabla^T N_I)\nabla N_J d\Omega \\ Q_{IJ} &= \int_\Omega \mathbf{B}_I^T \mathbf{m} N_J d\Omega \\ f_{\tau_I} &= \int_{\Gamma_t} \tau N_I \left[\rho\frac{Dv_n}{Dt} - \frac{2}{h_n}(2\bar{\mu}\,d_n - t_n)\right] d\Gamma - \int_\Omega \tau\nabla^T N_I b d\Omega \end{aligned} \tag{A.6}$$

where Γ_t are the free-surface contours of the domain, $m = [1,1,0]^T$ and τ is the stabilization parameter defined as in Oñate et al. (2014)

$$\tau = \left(\frac{8\bar{\mu}}{h^2} + \frac{2\rho}{\delta} \right)^{-1} \tag{A.7}$$

being h and δ characteristic distances in space and time (Oñate et al., 2014).

Acknowledgements This research was supported by the Spanish Ministry of Economy and Competitiveness (Ministerio de Economia y Competitividad, MINECO) through the Severo Ochoa Programme for Centres of Excellence in R&D (CEX2018-000797-S) and the project PRECISE (BIA2017-83805-R), the CARIPLO Project 2016-0769 - DARFLIS-Distributed quantitative risk Analysis for Rapid Flow-like Landslides induced by high Intensity Storms, the Project MIUR – Dipartimenti di Eccellenza 2018–2022, and the PRIN2017 project XFAST-SIMS: Extra fast and accurate simulation of complex structural systems (D41F19000080001).

References

Alonso, E., Pinyol, N., 2010. Criteria for rapid sliding I. a review of Vajont case. Eng Geol 114(3), 198–210.

Andersen, S., Andersen, L., 2010. Modelling of landslides with the material-point method. Computational Geosciences 14, 137–147.

Blikra, L., Longva, O., Harbitz, C., Løvholt, F., 2005. Quantification of rock-avalanche and tsunami hazard in storfjorden, Western Norway. volume In: Flaate K, Larsen J, Senneset K (eds.). Landslides. ICFL 2005 Norway. CRC press.

Bloom, C., MacInnes, B., Higman, B., Shugar, D., Venditti, J., Richmond, B., Bilderback, E., 2019. Catastrophic landscape modification from a massive landslide tsunami in Taan Fiord, Alaska. Geomorphology 107029.

Bosa, S., Petti, M., 2011. Shallow water numerical model of the wave generated by the Vajont landslide. Environmental Modelling & Software 26, 406–418.

Bosa, S., Petti, M., 2013. A numerical model of the wave that overtopped the Vajont dam in 1963. Water Resources Management 27, 1763–1779.

Braathen, A., Blikra, L., ansd F. Karlsen, S.B., 2014. Rock slope failures of norway; type, geometry, deformation mechanism and stability. Norwegian Journal of Geology 84, 67–88.

Brezzi, F., Fortin, M., 1991. Mixed And Hybrid Finite Element Methods. Springer, New York.

Broili, L., 1967. New knowledges on the geomorphology of the vaiont slide slip surfaces. Rock Mech. Eng. Geol. 5, 38–88.

Caloi, P., 1966. L'evento del Vajont nei suoi aspetti geodinamici. Instituto Nazionale di Geofisica, Roma.

Chen, S., Doolen, G., 1998. Lattice boltzmann method for fluid flows. Annual review of fluid mechanics 30, 329–364.

Ciabatti, M., 1964. La dinamica della frana del Vaiont. volume XXXII (I). Giornale di Geologia.

Cremonesi, M., Ferri, F., Perego, U., 2017. A basal slip model for lagrangian finite element simulations of 3D landslides. International Journal for Numerical and Analytical Methods in Geomechanics 41, 30–53.

Cremonesi, M., Franci, A., Idelsohn, S., Oñate, E., 2020. Review of the Particle Finite Element Method. Archives of Computational Methods in Engineering https://doi.org/10.1007/s11831-020-09468-4.

Cremonesi, M., Frangi, A., Perego, U., 2011. A Lagrangian finite element approach for the simulation of water-waves induced by landslides. Computer and Structures 89, 1086–1093.

Crosta, G., Imposimato, S., Roddeman, D., 2006. Continuum numerical modelling of flow-like landslides. NATO Science Series, Earth and Environmental Science. In: Evans SG, Scarascia Mugnozza G, Strom A, Hermanns R (eds) NATO ARW, Landslides from massive rock slope failure 49, 211–232.

Crosta, G., Imposimato, S., Roddeman, D., 2009. Numerical modeling of 2D granular step collapse on erodible and nonerodible surface. Journal of Geophysical Research: Earth Surface 114.

Crosta, G., Imposimato, S., Roddeman, D., 2016. Landslide spreading, impulse water waves and modelling of the Vajont rockslide. Rock Mechanics and Rock Engineering 49(6), 2413–2436.

Cundall, P., Strack, O., 1979. A discrete numerical model for granular assemblies. Géotechnique 29 (1), 47–65.

Datei, C., 1969. Su alcune questioni di carattere dinamico relative ad un eccezionale scoscendimento di un ammasso roccioso. Memorie della Accademia Patavina, Padova.

Dilley, M., Chen, R., Deichmann, U., Lerner-Lam, A., Arnold, M., Agwe, J., Buys, P., Kjekstad, O., Lyon, B., Yetman, G., 2005. Natural disaster hotspots: a global risk analysis. The World Bank Hazard Management Unit, Washington.

Edelsbrunner, H., Mucke, E., 1999. Three dimensional alpha shapes. ACM Transactions on Graphics (TOG) 13 (1), 43–72.

Edelsbrunner, H., Tan, T., 1993. An upper bound for conforming delaunay triangulations. Discrete and Computational Geometry 10 (2), 197:213.

Ferri, F., Toro, G.D., Hirose, T., Han, R., Noda, H., Shimamoto, T., Rossi, N.D., 2011. Low-to-high-velocity frictional properties of the clay-rich gouges from the slipping zone of the 1963 Vaiont slide, northern italy. Journal of Geophysical Research: Solid Earth 116:B09208.

Franci, A., Cremonesi, M., 2017. On the effect of standard PFEM remeshing on volume conservation in free-surface fluid flow problems. Computational Particle Mechanics 4 (3), 331–343.

Franci, A., Cremonesi, M., Perego, U., Oñate, E., Crosta, G., 2020. 3D simulation of Vajont disaster. part 2: Multi-failure scenarios. Submitted to Engineering Geology .

Franci, A., Oñate, E., Carbonell, J., 2015. On the effect of the bulk tangent matrix in partitioned solution schemes for nearly incompressible fluids. International Journal for Numerical Methods in Engineering 102 (3-4), 257–277.

Franci, A., Zhang, X., 2018. 3D numerical simulation of free-surface Bingham fluids interacting with structures using the PFEM. Journal of Non-Newtonian Fluid Mechanics 259, 1–15.

Fritz, H., 2002. Initial phase of landslide generated impulse waves. Swiss Federal Institute of Technology Zürich PhD thesis.

Fritz, H., Hager, W., Minor, H., 2001. Lituya bay case: rockslide impact and wave run-up. Sci Tsunami Hazards 19(1), 3–22.

Fritz, H., Mohammed, F., Yoo, J., 2009. Lituya bay landslide impact generated mega-tsunami 50th anniversary. Pure and Applied Geophysics 166(1–2), 153–175.

Froude, M., Petley, D., 2018. Global fatal landslide occurrence from 2004 to 2016. Natural Hazards and Earth System Science 18, 2161–2181.

Gauthier, D., Anderson, S., Fritz, H., Giachetti, T., 2018. Karrat fjord (Greenland) tsunamigenic landslide of 17 june 2017: Initial 3D observations. Landslides 15(2), 327–332.

Ghetti, A., 1962. Esame sul modello degli effetti di un'eventuale frana nel lago-serbatoio del Vajont. Costruzioni Idrauliche dell'Università di Padova. Centro modelli idraulici E. Scimemi S.A.D.E. Rapporto interno inedito 10, 23.

Ghirotti, M., 2012. The 1963 Vaiont landslide, Italy. JJ Clague, Stead D (eds) Landslides: types, mechanisms and Modeling.

Gingold, R., Monaghan, J., 1977. Smoothed particle hydrodynamics - theory and application to non-spherical stars. Monthly Notices of the Royal Astronomical Society 20, 375–389.

Haque, U., Blum, P., da Silva, P., Andersen, P., Pilz, J., Chalov, S., Malet, J., Auflič, M., Andres, N., Poyiadji, E., Lamas, P., Zhang, W., Peshevski, I., Pétursson, H.G., Kurt, T., Dobrev, N., García-Davalillo, J., Halkia, M., Ferri, S., Gaprindashvili, G., Engström, J., Keellings, D., 2016. Fatal landslides in europe. Landslides .

Haque, U., da Silva, P., Devoli, G., Pilz, J., Zhao, B., Khaloua, A., Andersen, P., Lu, P., Lee, J., Yamamoto, T., Keellings, D., Wu, J., Glass, G., 2019. The human cost of global warming: Deadly landslides and their triggers (1995–2014). Science of the Total Environment 673.

Harbitz, C., Glimsdal, S., Løvholt, F., Kveldsvik, V., Pedersen, G., Jensen, A., 2014. Rockslide tsunamis in complex fjords: From an unstable rock slope

at Åkerneset to tsunami risk in western norway. Coastal Engineering 88, 101–122.

Hendron, A., Patton, F., 1985. The Vaiont slide, a geotechnical analysis based on new geological observations of the failure surface. volume Tech Rep GL-85–5, vol 2. Department of the Army, US Corps of Engineers, Washington, DC.

Hirt, C., Nichols, B., 1981. Volume of fluid (VOF) method for the dynamics of free boundaries. Journal Computational Physics 39, 201–225.

Idelsohn, S., Calvo, N., Oñate, E., 2003. Polyhedrization of an arbitrary point set. Computer Methods in Applied Mechanics and Engineering 92 (22–24), 2649–2668.

Idelsohn, S., Marti, J., Limache, A., Oñate, E., 2008. Unified Lagrangian formulation for elastic solids and incompressible fluids: Applications to fluid-structure interaction problems via the PFEM. Computer Methods In Applied Mechanics And Engineering 197, 1762–1776.

Idelsohn, S., Oñate, E., Pin, F.D., 2004. The particle finite element method: a powerful tool to solve incompressible flows with free-surfaces and breaking waves. International Journal for Numerical Methods in Engineering 61, 964–989.

Larese, A., Rossi, R., Oñate, E., Idelsohn, S., 2008. Validation of the particle finite element method (PFEM) for simulation of free surface flows. International Journal for Computer-Aided Engineering and Software 25, 385–425.

Larese, A., Rossi, R., Oñate, E., Idelsohn, S., 2012. A coupled PFEM–Eulerian approach for the solution of porous fsi problems. ComputationalMechanics 50(6), 805–819.

Manenti, S., Amicarelli, A., Todeschini, S., 2018. WCSPH with limiting viscosity for modeling landslide hazard at the slopes of artificial reservoir. Water 10 (4), 515.

Manenti, S., Pierobon, E., Gallati, M., Sibilla, S., D'Alpaos, L., Macchi, E., Todeschi, S., 2016. Vajont disaster: Smoothed particle hydrodynamics modeling of the postevent 2D experiments. Journal of Hydraulic Engineering 142 (4), 0501500.

McDougall, S., Hungr, O., 2004. A model for the analysis of rapid landslide motion across three-dimensional terrain. Canadian Geotechnical Journal 41 (6), 1084–1097.

Miller, D., 1960. Giant waves in lituya bay alaska. USGS Prof. Paper 354-C, 51–83.

Minatti, L., Pasculli, A., 2011. SPH numerical approach in modelling 2D muddy debris flow. International Conference on Debris-Flow Hazards Mitigation: Mechanics, Prediction, and Assessment , 467–475.

Muller, L., 1964. The rock slide in the Vajont valley. Felsmechanik und Ingenieur Geologie.

Mulligan, R., Franci, A., Celigueta, M., Take, W., 2020. Simulations of landslide wave generation and propagation using the Particle Finite Element Method. Journal of Geophysical Research: Oceans 125, e2019JC015873.

Nonveiller, E., 1987. The Vajont reservoir slope failure. Engineering Geology. Dam Failures 24, 493 – 512.

Osher, S., Fedkiw, R., 2002. Level set methods and dynamic implicit surfaces. Springer.

Oñate, E., 1998. Derivation of stabilized equations for advective-diffusive transport and fluid flow problems. Computer methods in applied mechanics and engineering 151, 233–267.

Oñate, E., Franci, A., Carbonell, J., 2014. Lagrangian formulation for finite element analysis of quasi-incompressible fluids with reduced mass losses. International Journal for Numerical Methods in Fluids 74 (10), 699–731.

Oñate, E., Idelsohn, S., Pin, F.D., Aubry, R., 2004. The particle finite element method. An overview. International Journal for Computational Methods 1, 267–307.

Pak, A., Sarfaraz, M., 2014. Lattice boltzmann method for simulating impulsive water waves generated by landslides. Transactions on Civil Engineering (A), Scientia Iranica , 318–328.

Papanastasiou, T., 1987. Flows of materials with yield. Journal of Rheology 31, 385–404.

Paris, A., Guérin, E., Heinrich, P., Schindelé, F., Hébert, H., 2019. Numerical modeling of the june 17, 2017 landslide and tsunami events in Karrat fjord, west Greenland. Pure and Applied Geophysics 176(7), 3035–3057.

Paronuzzi, P., Rigo, E., Bolla, A., 2013. Influence of filling–drawdown cycles of the Vajont reservoir on mt. toc slope stability. Geomorphology 191, 75–93.

Pastor, M., Blanc, T., Haddad, B., Drempetic, V., Morles, M., P, P.D., Stickle, M., Mira, P., Merodo, J., 2015. Depth averaged models for fast landslide propagation: mathematical, rheological and numerical aspects. Archives of Computational Methods in Engineering 22, 67–104.

Pastor, M., Haddad, B., Sorbino, G., Drempetic, V., 2009. A depth integrated, coupled SPH model for flow like landslides and related phenomena. International Journal for numerical and analytical methods in geomechanics 33, 143–172.

Pinyol, N., Alvarado, M., Alonso, E., Zabala, F., 2017. Thermal effects in landslide mobility. Géotechnique , 1–18.

Pouplana, I.D., Oñate, E., 2017. A FIC-based stabilized mixed finite element method with equal order interpolation for solid–pore fluid interaction problems. International Journal for Numerical and Analytical Methods in Geomechanics 41, 110–134.

Qiu, L., Tian, L., Liu, X., Han, Y., 2019. A 3D multiple-relaxation-time LBM for modeling landslide-induced tsunami waves. Engineering Analysis with Boundary Elements 102, 51–59.

Quecedo, M., Pastor, M., Herreros, M., 2004. Numerical modelling of impulse wave generated by fast landslides. International Journal for Numerical Methods in Engineering 59, 1633–1656.

Ratkowsky, D., 1990. Handbook of nonlinear regression models. Dekker, New York.

Rossi, D., Semenza, E., 1965. Carte geologiche del versante settentrionale del M. Toc e zone limitrofe, prima e dopo il fenomeno di scivolamento del 9 Ottobre 1963, Scala 1:5000. volume Le foto della frana del Vajont. Instituto di Geologia dell'Universitá di Ferrara.

Rossi, D., Semenza, E., 1986. Carta geologica del versante settentrionale del M. Toc e zone limitrofe. volume Le foto della frana del Vajont. Masè G, Semenza M, Semenza P, Semenza P, Turrini MC, 2004, Le foto della frana del Vajont.

Ryzhakov, P., Oñate, E., Idelsohn, S., 2012. Improving mass conservation in simulation of incompressible flows. International Journal of Numerical Methods in Engineering 90, 1435–1451.

Rzadkiewicz, S., Mariotti, C., Heinrich, P., 1997. Numerical simulation of submarine landslides and their hydraulic effects. Journal of Waterway, Port, Coastal, and Ocean Engineering 123 (4), 149–157.

Salazar, F., Irazabal, J., Larese, A., Oñate, E., 2016. Numerical modelling of landslide-generated waves with the particle finite element method (PFEM) and a non-Newtonian flow model. International Journal for Numerical and Analytical Methods in Geomechanics 40, 809–826.

Salazar, F., Oñate, E., Morán, R., 2012. Numerical modelling of lanslide flows on reservoirs with the particle finite element method (PFEM). Revista Internacional de Métodos Numéricos para Cálculo y Diseño en Ingeniería 28(2), 112–123.

Selli, R., Trevisan, G., 1964. La frana del Vaiont. volume Serie 2(32). Giornale di Geologia, Annali del Museo Geologico di Bologna.

Semenza, E., 1965. Sintesi degli studi geologici sulla frana del Vaiont dal 1959 al 1964. volume 16. Mem Mus Trident Sci Nat, A XXIX–XXX.

Semenza, E., 2002. La storia del Vajont. volume 2(32). Annali Mus Geol Serie.

Semenza, E., 2010. The story of Vajont told by the geologist who discovered the landslide. Tecnoproject, Ferrara.

Semenza, E., Ghirotti, M., 2010. History of 1963 Vaiont slide. the importance of the geological factors to recognise the ancient landslide. Bull Eng Geol Env 59, 87–97.

Shan, T., Zhao, J., 2014. A coupled CFD-DEM analysis of granular flow impacting on a water reservoir. Acta Mechanica 225(8), 2449–2270.

Sitar, N., MacLaughlin, M., Dolin, D., 2005. Influence of kinematics on landslide mobility and failure mode. Journal of geotechnical and geoenvironmental engineering 131 (6), 716–728.

Soga, K., Alonso, E., Yerro, A., Kumar, K., Bandara, S., 2016. Trends in large-deformation analysis of landslide mass movements with particular emphasis on the material point method. Géotechnique 66 (3), 248–273.

Sulsky, D., Chen, Z., Schreyer, H., 1994. A particle method for history-dependent materials. Computer Methods in Applied Mechanics and Engineering 118, 179–196.

Tika, T., Hutchinson, J., 1999. Ring shear tests on soil from the Vaiont landslide slip surface. Géotechnique 49(1), 59–74.

Vacondio, R., Mignosa, P., Pagani, S., 2013. 3D SPH numerical simulation of the wave generated by the Vajont rockslide. Advances in water resources 59, 146–156.

Viparelli, M., Merla, G., 1968. L'onda di piena seguita alla frana del Vajont. Università degli Studi di Napoli.

Voight, B., Faust, C., 1982. Frictional heat and strength loss in some rapid

landslides. Géotechnique 32, 43–54.
Ward, S., Day, S., 2008. Tsunami balls: A granular approach to tsunami runup and inundation. Communications in Computational Physics 10, 222–249.
Ward, S., Day, S., 2011. The 1963 landslide and flood at Vaiont reservoir italy. a tsunami ball simulation. Italian Journal of Geoscience 130 (1), 16–26.
Yerro, A., Pinyol, N., Alonso, E., 2016. Internal progressive failure in deep-seated landslides. Rock Mechanics and Rock Engineering 49, 2317–2332.
Yerro, A., Soga, K., Bray, J., 2019. Runout evaluation of the oso landslide with the material point method. Canadian Geotechnical Journal 56 (9), 1304–1317.
Zaniboni, F., Tinti, S., 2014. Numerical simulations of the 1963 Vajont landslide, italy: application of 1d lagrangian modelling. Natural hazards 70(1), 567–592.
Zhang, X., Krabbenhoft, K., Sheng, D., Li, W., 2015. Numerical simulation of a flow-like landslide using the particle finite element method. Computational Mechanics 55, 167–177.
Zhang, X., Oñate, E., Galindo, S., Bleyer, J., Krabbenhoft, K., 2019. A unified lagrangian formulation for solid and fluid dynamics and its possibility for modelling submarine landslides and their consequences. Computer Methods in Applied Mechanics and Engineering 343, 314–338.
Zhang, X., Sheng, D., Sloan, S., Bleyer, J., 2017. Lagrangian modelling of large deformation induced by progressive failure of sensitive clays with elastovis-coplasticity. International Journal for Numerical Methods in Engineering 112, 963–989.
Zhao, T., Utili, S., Crosta, G., 2016. Rockslide and impulse wave modelling in the Vajont reservoir by CFD-DEM analyses. Rock Mechanics and Rock Engineering 49(6), 2437–2456.
Zienkiewicz, O., Taylor, R., Nithiarasu, P., 2005. The Finite Element Method for Fluid Dynamics,Volume 3 (6th Ed.). Elsiever, Oxford.